In-situ monitoring of temperature distribution in operating solid oxide fuel cell cathode using proprietary sensory techniques versus commercial thermocouples

Erdogan Guk[a], Jung-Sik Kim[a,*], Manoj Ranaweera[b], Vijay Venkatesan[a], Lisa Jackson[a]

[a] Department of Aeronautical & Automotive Engineering, Loughborough University, Epinal Way, Loughborough LE11 3TU, United Kingdom
[b] Department of Mechanical Engineering, University of Moratuwa, Sri Lanka

HIGHLIGHTS

- A physical sensor is placed directly onto solid oxide fuel cell electrode.
- Temperature increment (0.4–3 °C) was monitored locally with varying fuel flow rate.
- Respective contributions of gas cooling, starvation and electrochemical activity investigated.
- The sensor presents higher temporal and spatial resolution than conventional TCs.
- All experimentally measured data were validated with theoretical calculations.

ARTICLE INFO

ABSTRACT

Real time surface temperature distribution monitoring of Solid Oxide Fuel Cell (SOFC) systems is important to identify temperature related degradation and understand cell performance. This type of monitoring is limited due to the harsh operating environment of SOFC. Therefore, the temperature variation of an operating SOFC is generally predicted by applying modelling tools which take into account the conventional I-V (current (I)-voltage (V)) curve. However, experimentally obtained temperature data is vital for management of high temperature related degradation and for more reliable modelling of the SOFC. In this study, the temperature distribution of the SOFC is *in-situ* monitored along the entire cell cathode simultaneously, using commercial TCs on the gas flow channel (the present conventional method) alongside the in-house-developed sensor sensing points (SSPs) directly from the cell cathode surface under both open circuit voltage (OCV) and loading conditions. A considerable difference is observed, especially under the loading condition, between the temperature obtained from the TCs and SSPs even from the same locations. Furthermore, the contribution(s) of different parameters on the temperature variation are investigated, including fuel/air amount under OCV, gas cooling effect, contact area effect and flow direction effect under the loading condition for the given SOFC. There is a fivefold increase in spatial resolution, alongside higher temporal resolution, being observed with the implemented sensor compared to the resolution obtained from the conventional TCs, which yields promise for further development and investigation into test cells and stacks.

1. Introduction

SOFCs, as highly efficient (> 50%) [1], energy conversion devices, have been considered as a promising technology to make important contributions to cover the power demand of the ever-growing society [2,3]. However, it faces the primary challenge of degradation issues due to its aggressive operating conditions, including high operating temperatures ranging from 600 °C to 1000 °C [4,5]. As a result of issues deriving from or related to the high operating temperature (such as thermal stress where thermal expansion mismatches induce cell cracking or delamination), there are several studies focussed on decreasing the operating temperature of SOFCs [6,7]. However, a high operating temperature provides some important benefits, such as lower overpotentials, resulting in higher power outputs, higher ionic and electronic conductivity, ability to use more economical catalyst materials, and offering a wider range of hydrocarbon usage [8]. In addition,

---

it provides the opportunity to be integrated with other high temperature systems (such as gas turbines, combined heat-power) resulting in an increase in its efficiency [9]. Therefore, understanding and managing the thermal properties of SOFCs is important and plays a key role in solving the high temperature drawbacks on SOFC performance without sacrificing the benefits.

Computational modelling is generally the preferred way to predict the temperature gradient of a working SOFC [10,11]. There are two strong reasons that facilitate the ease and applicability of numerical studies for analysing the SOFC operating parameters, compared to experimental measurement techniques (which include sensory (TCs, thermistors), electrochemical (electrochemical impedance spectroscopy (EIS), voltammetry) and optical technologies, Raman spectroscopy and Fourier transform infrared spectroscopy (FTIR)). The first is the harsh operating conditions, which is a limiting factor for many of the aforementioned optical measurement technologies, and the second is limited space, which restricts the implementation of measurements with sensory technologies [11]. Furthermore most of the optical techniques only focus on an analysis correlating temperature exclusively to electrochemical reaction(s); however, the cell's chemical reactions are also an important contributor to the heat release/sink in SOFC systems [12]. Advances with the integration of Sagnac interferometric optical set up and infrared thermometer (IR) was developed and used for SOFC surface in-situ temperature and deformation measurement at 800 °C [13]. Nevertheless, the system required more instrumentation and the obtained spatial resolution was poor. Most recently, IR imaging with integrated Matlab coding was performed to monitor the SOFC temperature during operation under different operating conditions [14]. The achieved temporal and spatial resolutions were satisfactory; however, the limited accessibility to the electrode for optical imaging is a challenging obstacle for stack-level SOFC operations. Therefore, with the need for greater understanding of the SOFC system and a concurrent development in computing capabilities, there is increasing interest in SOFCs from the vantage of modelling-based research by using different approaches to obtain the most suitable and accurate approximations [15]. On the one hand, investigations from numerical modelling are important in estimating the possible temperature distribution, as well as failure mechanisms, especially for predictions over extended time durations (> 40,000 h). On the other hand, present validation of SOFC models are performed by considering only the conventional I-V curve and its correlation with the spatial current; this is insufficient to explore accurately the temperature characteristics [16]. Hence in-situ temperature distribution measurement is still vital not only for real time temperature monitoring but also for validation of the computational methodologies and their findings to improve its reliability.

Although the SOFC system is a taxing environment for implementation of sensory techniques within the cell or stack during operation, TCs are still the most common experimental technique for serving the purpose of temperature gradient measurement [13,17]. Due to its wider working temperature range, coupled with lower cost, K-type TCs are used by many researchers for SOFC systems [18]. When using a sensing technique, awareness of the uncertainty of the contributions of other heat sources (including heat flux due to radiation and heat released or absorbed by electrochemical reactions that take place during SOFC operation) is needed. Furthermore, there are other parameters, such as, gas flow types and gas feed temperature that might affect the sensor reading, depending on the proximity of those sources to the sensing devices. Therefore, there is a divergence on the reliability of temperature distribution measurement obtained by using TCs since the TCs are generally located in the flow channel. Ju et al. [19] claim that the measured temperature via the TCs from the flow channel, which is generally placed only 2–3 mm above the cell surface, is not only due to the cell activities itself, but rather can be compounded with the heat flux-induced temperature inside the manifold with contributions from the product gases, furnace heating element and cell activity.

With regards to the importance of thermal management of SOFC

and the issues on the current measurement techniques, in this study, the temperature distribution measured with a recently developed sensor is taken directly from the SOFC cell surface. A different version of the sensor has been used for SOFC temperature monitoring by the authors [18,20]. In the current experiment, two commercial TCs located close to two of the SSPs were also used. The measurement from the commercial TCs and SSPs were obtained under loading and OCV conditions. During SOFC cell operation the response of the TCs and SSPs to temperature variations of the cell was monitored and the data obtained from both is compared in order to investigate temporal and spatial resolution of the sensors in comparison with the TCs. To the author's best knowledge, there are no available experimental studies in the literature to validate the reliability of the TCs' temperature measurements. Given that TC-based measurement is widely applied for the validation of modelling based measurements, the obtained results from this research will contribute to both areas, alongside identifying the differences between the measurements and the parameters leading to those differences.

2. Experimental process

2.1. Materials

A planar, anode-supported SOFC test specimen, measuring 50 mm × 50 mm (FuelCellStore, USA) is used for the experiment. The cell consists of a 500–600 μm thick Ni-YSZ (Nickel-Yttria Stabilized Zirconia) anode, 7–10 μm thick YSZ electrolyte, a 3–5 μm thick GDC (Gadolinium Doped Ceria) intermediate layer and a 30–60 μm thick Lanthanum strontium cobalt ferrite (LSCF) /LSCF-GDC cathode.

A self-designed counter-flow manifold, made from Macor™ machineable ceramic, was used in this experiment. Vermiculite-type gaskets with thickness of 0.5 mm were used for sealing (Flexitallic Ltd Thermiculite 866). The cell was sandwiched between two gaskets to hinder any unwanted gas leakage. Alumina paste (Aremco products, Ceramobond-552) was applied at the junction to mount the sensor thermoelements on the cathode. Silver meshes (PI-KEM Ltd) were used on both sides of the cell as a current collector, with a silver paste (Sigma-Aldrich) to bond the meshes on the electrodes. LabVIEW software was used for data collection (National Instruments Corporation Ltd. U.K.). Alumel and chromel wires, with thicknesses of 0.25 mm in diameter (PI-KEM Ltd), were used as the sensor thermoelements to form K-type TCs at each junction. The working principle of the sensor is similar to the commercial TCs which work depending on the Seebeck theory (1) [21].

$$V_{emf} = \int_{T0}^{T1} (S_A - S_B) dT \tag{1}$$

where V_{emf} is the Seebeck potential converted to a corresponding temperature, S_A and S_B are the Seebeck coefficients of the two used thermoelement materials (alumel and chromel), T1 is the temperature at the junction (hot reference) and T0 is the temperature at the outside (cold reference).

The cell-embedded sensor has an important advantage of requiring less thermoelements in comparison to commercial TCs even for the same number of sensing points due to its architecture. The architecture of the sensor is a driving factor for creating independent sensing points. In this study, a grid architecture comprising of four alumel and four chromel thermoelements, resulting in sixteen independent sensing points, was used as depicted in the Fig. 1. Spot welding technique is applied for joining the wires to create required junctions. The accuracy and precision is a vital requirement for thermocouples especially for such sensitive measurement. The main parameter that dominates the accuracy is the Seebeck coefficient of the thermoelements which varies upon changes of the material compositions of the thermoelements. The K-type thermocouples are commonly used up to 1200 °C with allowed error ranges, ie ± 1–3 °C at the given range based on ISO. Therefore the
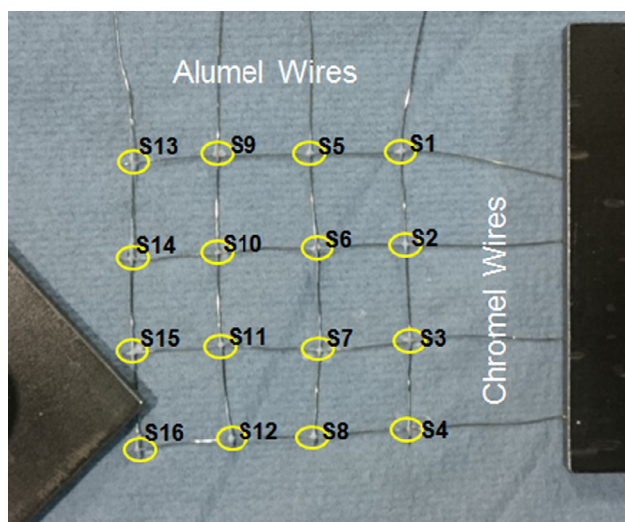
Fig. 1. Spot welded grid sensor architecture.

Fig. 2. Schematic representation of the inserted sensor sensing points and cell cathode configuration (not to scale).

authors do not expect a critical Seebeck coefficient based error. Furthermore due to different fabrication of the customised sensor even though it has been calibrated with the certificated commercial thermocouple, there can be a difference in the expected obtained temperature due to different resistance created through the electrical circuit. However, due to the Seebeck theory the impact of the internal resistance effect is negligible as it is assumed that there is a negligible amount of current flow in the thermocouples circuit and thus the Seebeck coefficient and temperature changes are the only parameters leading to changes in the obtained temperature measurement [21].

The fabricated SSPs are directly mounted on the cathode electrode by applying tiny amounts of alumina on the junctions to physically bond the sensor on to the electrode as well as preventing possible electrical interaction between sensor thermoelements and the cathode. Therefore, the SSPs are in direct physical contact with the cathode surface via alumina, an electrically non-conductive media, throughout the experiments. With this set up it is hoped that the sudden temperature variation caused by cell electrochemical and chemical activities are captured as soon as the heat is released. Depending on the location of the SSPs, the released heat from the cell activities can be altered if there is non-uniform temperature occurrence in the measuring environment. The supplied gases, heat fluctuation in the furnace and radiation due to the furnace heating element are potential influences that can cause temperature fluctuation from the baseline operating SOFC cell temperature. For this reason, it is crucial to have a temperature sensing capability with higher temporal and spatial resolution to obtain a more reliable temperature distribution of the cell activities.

2.2. Cell-Sensor-manifold configuration

Fig. 2 shows the schematic view of the SSPs implemented on a transparent cell which is placed on the anode compartment of the manifold with silver mesh (current collector) and silver paste. The locations of the SSPs, fuel and air inlets and outlets and the two commercial TCs are also shown in Fig. 2. It is ensured that there is no electrical contact between sensor and cathode electrode and no physical contact with the current collector. TC1 (thermocouple 1) and TC2 (thermocouple 2) are located close to S1 and S13, just 2–3 mm above the electrode surface, respectively. The potential electrical interference between the TCs and implemented sensor is also checked and secured before the experiment. Fuel inlet and outlet holes are represented with the dashed circle in the top-left and bottom-right respectively while air inlet and outlet holes are represented with solid circles in the bottom-left and top-right respectively in Fig. 2. The counter-flow field
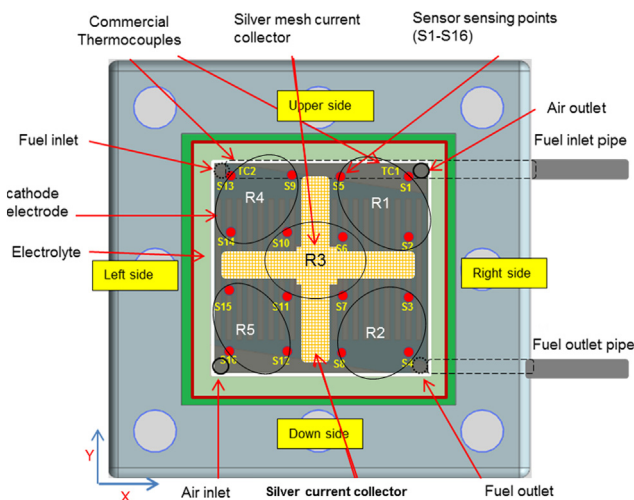
configuration is achieved, though difficult to view in 2D. The air enters from the bottom left and exits from top right, whilst the situation is reversed for the fuel side (Fig. 2).

The active area of the cell is originally $16 \, cm^2$; however only $\sim 3 \, cm^2$ area (current collection area) is covered by the current collector. A less influential factor is the electrode area covered by the sensor attachment points which are estimated to cover a total area of $0.34 \, cm^2$ (10 sensing points at $1 \, mm^2$ + 6 sensing points at $4 \, mm^2$ = approx. $34 \, mm^2$). Therefore, a loss is incurred in the collection of all current from electrode interface to the current collector, especially for a thin cathode layer ($< 10 \, \mu m$), which eventuates in obtaining low power output [22]. Nonetheless, reaching the maximum or optimum power output is not the main focus of this study. There are two main reasons for using a smaller-sized, plus-shaped current collector. First, to clearly identify/monitor the effect of electrical contact points (the area covered by external current collection) on local temperature distribution, achieved by deliberately applying a non-uniform current collector across the entirety of the electrode surface (the area is also limited by the implemented wire-type SSPs). Second, the plus shape is used to create a symmetric distribution of SSPs with respect to the current collector at all sides of the electrode which allows us to identify/monitor the impact of the air and fuel supply effects, including their cooling effects and utilisation-related effects on local temperature distribution. In the stack-level SOFC system (and also with single cell testing), the current collector touches the electrode surface at certain points (only the ribs of interconnect) depending on the design of interconnect; in other words, there is a discrepancy between the cell active area and current collection area. The free active area is usually used to have an effective reactant transfer to entire surface of a cell. Thus, there is a great interest in understanding the impact of the current collector materials and its forms (paste or grid) on SOFC performance in the literature [23]. However, the effect of the current collection area on both overall temperature distribution across the entire electrode surface, as well as the temperature distribution between the local regions occupied by the current collector and nearest free region, has not been studied yet. In this study, with the implemented current collection mechanism it might be possible to observe the temperature distribution due to fuel-air effects and contact point effects under the given experimental conditions.

2.3. SOFC anode reduction and operation

After the whole assembly was completed, including sensor and cell electrical connections, the assembled manifold was placed in a high
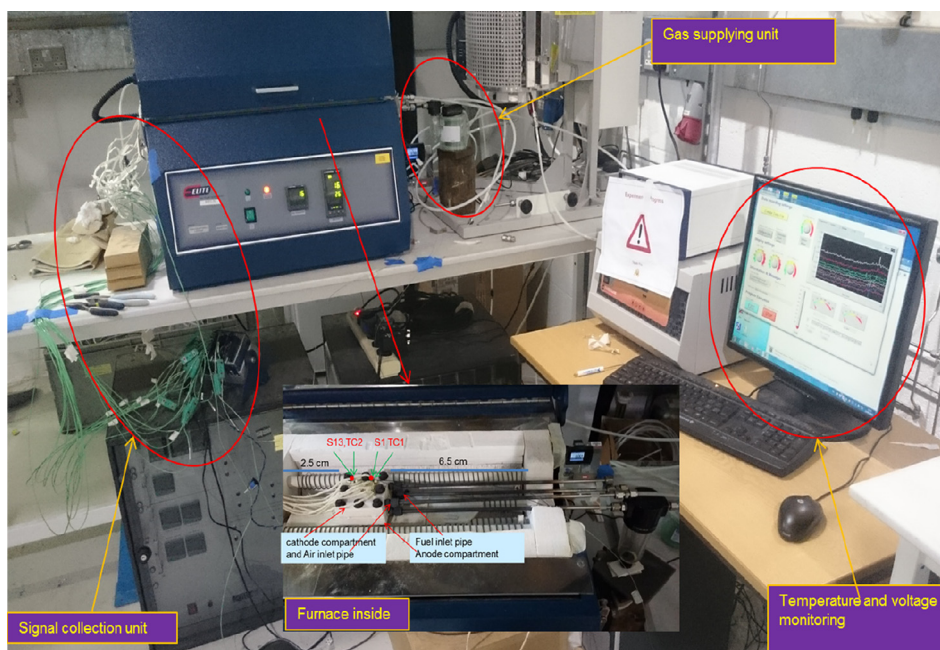
Fig. 3. Experimental set up consisting of supplying, signal collecting, monitoring units and manifold placed furnace.

temperature horizontal furnace as seen in Fig. 3. The horizontal furnace has two open sides on the right and on the left to insert the required pipes and/or external wires within the furnace (the left is not clearly shown but is where the beaded wires exit). The open parts of the furnace are then closed with an insulating material (thermal fibre), though it is expected that more heat loss, via convection and conduction, can occur at the points closer to these sealed parts due to the high temperature difference between the furnace and ambient atmospheres. As a result, there can be a temperature difference within the furnace, with lower temperatures measured near the wall, or sealed parts, compared to the central parts of the furnace. It is expected that the manifold and the cell inside the manifold are also affected by this temperature variation. As a result, a local temperature gradient may occur on the manifold as well as along the entire cell surface in differing ranges depending on the thermal inertia of each component. The placement of the manifold in the furnace is shown in the Fig. 3 where the manifold is 2.5 cm away from the left wall and is 6.5 cm away from the right wall. The possible impact from the factors correlated with the furnace specification, and design and placement of the manifold on temperature distribution is considered in the analysis to distinguish the sources of the released heat.

Once all the required gas pipes, including Nitrogen (N_2), Hydrogen (H_2) and Air, were equipped with the corresponding inlets and outlets of the manifolds, the furnace was closed and sealed. The furnace temperature was increased to first 250 °C (2 °C min^{-1}) and dwelled for two hours at that temperature for curing purposes of the applied silver and alumina pastes. It was then increased to 750 °C (2 °C min^{-1}) to start the anode reduction process which is required prior to cell operation. N_2 gas (75 mL min^{-1}) was constantly sent to the anode chamber throughout heating as well as during the experiment process to prevent any redox reaction. When the furnace temperature reached 750 °C, H_2 was sent together with N_2 at a flow rate of 50 mL min^{-1} for the anode reduction process for a period of 10 h. After the reduction process was completed the furnace temperature was increased to 800 °C with the same heating rate for testing the cell performance and temperature distribution under real operating conditions. All the sensor wires were connected to the data logging system where the LabVIEW programme performed the data acquisition. The data for temperature measurement and cell voltage measurement were recorded in the same interval simultaneously by the same data logging system. For conditions

involving loading, an electrochemical test station (Solartron© 1280C FRA + Potentiostat) was used, in conjunction with a CorrWare™ suite to log voltage and current, with the LabView programme running in parallel. The arrangement utilised a two-probe setup, with the working electrode set to the anode.

3. Results and discussions

3.1. Temperature distribution under OCV condition

Fig. 4 shows the temperature distribution from both SSPs (S1-S16) and TCs (TC1-S1 and TC2-S13) under OCV conditions with two different H_2 flow rates of 25 mL min^{-1} and 50 mL min^{-1}. The experimentally obtained OCV (Vexpr) (1.07 V) is comparable to the value available in the literature as well as in good agreement with the theoretical OCV (Vtheor) (1.09 V) which is slight higher than the experimental OCV. The furnace set temperature was 800 °C and this was maintained during the experiment.

As can be observed from Fig. 4, there is roughly a 2.5 °C difference between the TCs readings, in which the temperature of TC1 is slightly higher than 803 °C while TC2 is at about 800.5 °C with the flow rate of 25 mL min^{-1}. Also there are no visible changes observed in temperature difference between the obtained temperature from TC1 and TC2 with the increase in flow rate; in other words, both TC1 and TC2 readings increased the by the same amount with the increase in flow rate. In contrast, the maximum temperature differences in readings from the SSPs were about 1.25 °C with the 25 mL min^{-1} H_2 flow rate and the variation decreased to about 1 °C with the increased flow rate. As seen from Fig. 2, TC1 is located close to S1 and TC2 is close to S13 and the manifold is placed closer to the left side of the furnace (Fig. 3). All the measurements with S13-S16 are less than the measurement obtained from the other SSPs, as they are located on the left side of the manifold, which is where the fuel and air inlets are placed (Fig. 2). The obtained temperatures from S1-S8, as they are the highest with a small difference between themselves and the recorded measurement of S9-S12 as depicted in Fig. 4. As can be seen from Fig. 4, there is a lower temperature observed from the SSPs located to left side of the cell which is where the air and fuel inlets are than the temperature obtained from the SSPs closer to the air and fuel outlet which is to the right side of the cell. This can be caused mostly due to the location of the
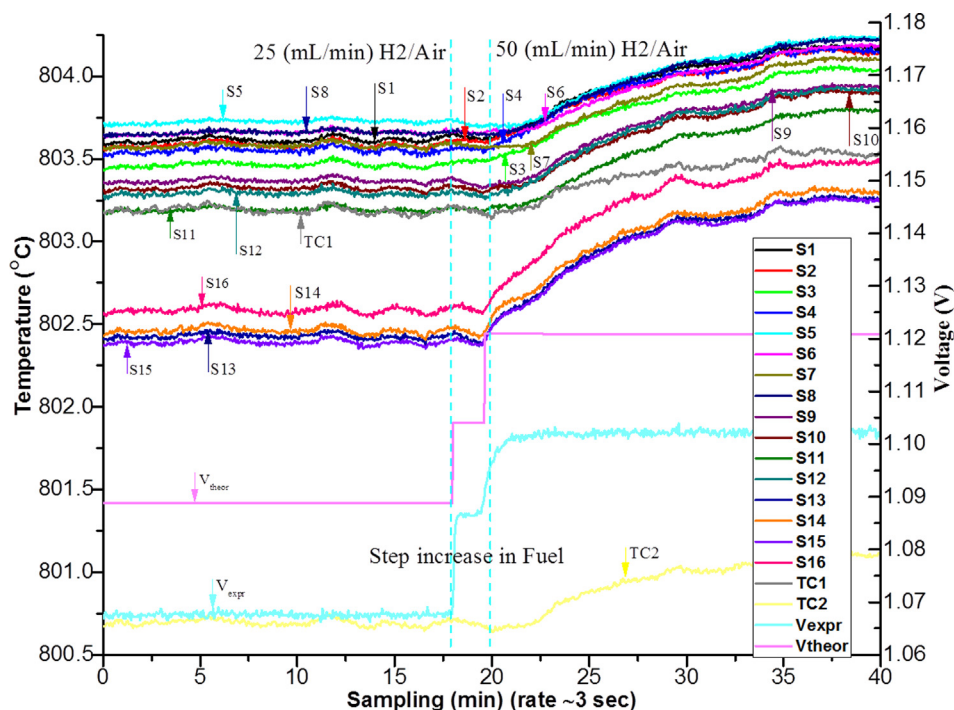
Fig. 4. Temperature monitoring from sixteen sensing point with sensor and two TCs under OCV conditions with different flow rates.

manifold as it closer to the furnace wall on the left side, thus experiencing relatively more heat loss via sealing. In addition to this, the fuel cooling effect can be another reason for obtaining lower temperature from the SSP readings located near the inlets, which will be discussed further in the section covering cell operation under load. Similar behaviour is also seen from TC1 and TC2 where TC1, which is located to the right center of the manifold, shows a higher temperature than TC2 which is located to the left side of the manifold (closer to the fuel and inlet points). The effect due to the manifold position can be attributed to non-uniform temperature distribution between the furnace center and the points closer to the furnace wall as seen in Fig. 3.

As represented in the result shown in Fig. 4 the obtained temperature difference in the TCs (2.5 °C) is higher than the difference in the corresponding SSPs (S13 and S1) (1 °C) under OCV conditions. This is due to the difference in thermal inertia between the gases in the flow channel (where the TCs capture the reading) and the cell surface (where the SSPs capture the readings).

It is also important to analyse the temperature increments of each sensing point with the raised flow rate for deeper understanding of temperature distribution across the cell surface. Regarding this point, the surface profile of the temperature increments of each SSP, with the increase in flow rate from 25 to 50 mL min^{-1} is illustrated in Fig. 5. To observe the increments of each SSP it is important to identify the heat sources leading to these temperature variations.

As seen from Fig. 5, there are similar temperature increments (∼0.6 °C) obtained from S1-S12 with a small variation among them. The maximum increments (∼1 °C), on the other hand, are monitored from S13-S16 located close to the fuel and air inlets (left side of the cell). Additionally, even though, the minimum increment (0.4 °C) is obtained with the TCs, they show a similar behaviour to the SSPs as the TC2 located near the gas inlets show higher increments than the TC1 located closer to the air and fuel outlets (right side) (Fig. 4). There can be three reasons for temperature increase with flow rate. The first reason is small gas (H$_2$) leakage from the anode to the cathode via the gasket leading to direct oxidation of H$_2$ with the air at the cathode side near the outer side of the cell. Despite the purpose- built cell holders being checked in terms of gas leakages before experimentation, there is still the potential for a marginal level of gas leakage when considering

SOFC operating conditions. It is proved by the result depicted in Fig. 5, as the average increments monitored from the SSPs located around the outer side of the cell/nearby gasket (specifically at the gas inlets) are higher than the average increments obtained from the sensing points located at the inner side of the cell (see Fig. 2 for SSPs locations). In addition to this, the gas leakage via electrolyte is less likely since OCV (Vexpr) reached its expected value of 1.1 V [24]. The second reason can be the oxidation reactions taking place between the supplied H$_2$ and preoccupied oxygen from the anode reduction process. Even though the microstructure changes of the anode due to NiO/Ni reduction has been studied [25,26] there is no study available in the literature specifically focused on the remaining oxygen from the reduction process. The final reason can be attributed to electronic current leakages as it is difficult to avoid electronic conduction of electrolytes at high operating temperatures (especially with a ceria-containing electrolyte) [27]. Those electrons allow oxygen to be reduced at the cathode resulting in oxygen ions. These ions are kinetically active enough to travel to the anode at this operating temperature. There is an oxidation reaction taking place at the anode when these oxygen ions meet with hydrogen leading to a heat release. The starting point of the circle is electronic current leakages which has a direct relation with the amount of supplied fuel. The reason for the lower increment obtained from the TCs in comparison with the corresponding SSPs located near them, is due to distance to the heat sources. Most likely the direct oxidation reaction takes place in the porous cathode electrode that is first detected by the SSPs which are in direct contact with the electrode surface. It is also important to note that the response time (temporal resolution) of S13-S16 near to the inlet side to the temperature changes is 2–3 min quicker than TC2 which is located close to S13.

3.2. Thermodynamic analysis of obtained cell temperature and voltage

As illustrated in Fig. 4 the obtained experimental OCV increased gradually with the step increase in fuel flow rate due to the increase in partial pressure. In order for the comparison, Nernst equation, as shown in Eq. (2), is performed for the theoretical calculation of the OCV. As seen from Fig. 4 there is good agreement between experimentally (Vexpr) and theoretically (Vtheor) obtained OCV values as they both
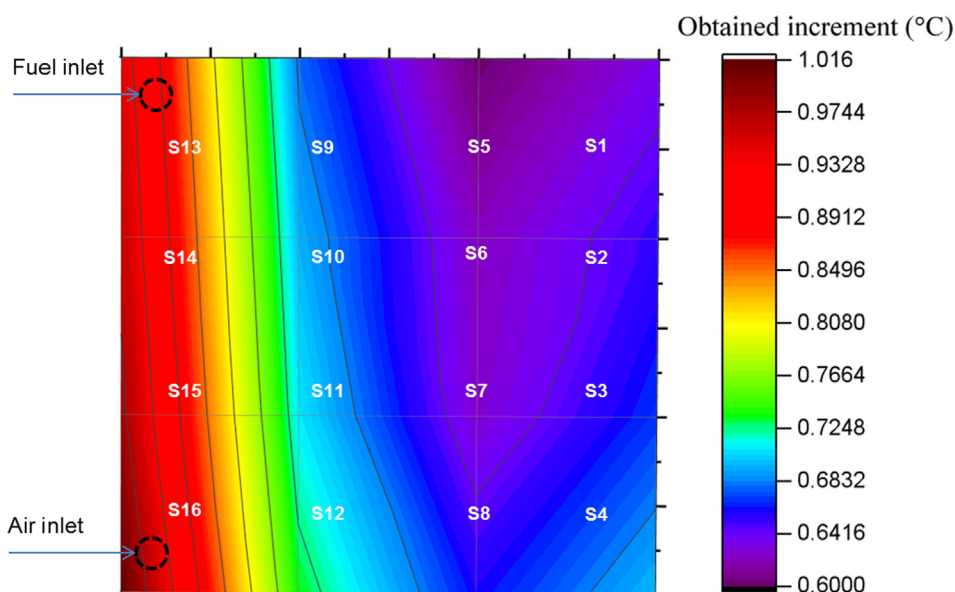
Fig. 5. Increment in temperature with the increase in flow rate under OCV condition.

agree with the value available in the literature [24].

$$E = E° + \frac{RT}{nF}\ln\left(\frac{P_{H_2}\cdot P_{O_2}^{1/2}}{P_{H_2O}}\right) \tag{2}$$

where E is the operating OCV, $E°$ is the OCV at fuel cell operating temperature and standard pressure (1 atm), n is the moles of electrons released for every mole of H_2 reacted (2 mol e⁻ mol⁻¹ H_2), F and R is Faraday and gas constant respectively, P_{H_2}, P_{O_2} and P_{H_2O} are the partial pressure of reactant and product respectively.

According to the Nernst equation, there is an inverse relation between cell V_{theor} and operating temperature due to a decrease in Gibbs free energy with the increase in temperature, while it increases with the increase in reactant partial pressure [17]. The obtained result shown in Fig. 5 agrees with this as the V_{expr} increased with the step increase in H_2 fuel/air flow rate. However, there is an increase also observed in temperature and this is something that cannot be straightforwardly explained by the thermodynamic aspects of an SOFC system, given that the reason for the increase in temperature with fuel flow rate is most likely due to H_2 leakage to the cathode side generating direct oxidation of H_2 as aforementioned, which is not accounted for in the thermodynamics of SOFCs. Additionally, one of the possible reasons could be the oxidation reaction taking place at the anode side between the preoccupied oxygen and supplied H_2, as the partial pressure increased with the increase in flow rate. The effect of increased H_2 partial pressure can also be seen from the changes in V_{expr} and V_{theor} as depicted in Fig. 4. Thus, there is no simultaneous change between temperature and measured OCV. Even though the OCV increased immediately, as soon as the fuel rate increased, the increase in cell temperature (from all SSPs) was only monitored with an interval of time scale which is explained in detail in Section 3.4. Moreover, both the V_{expr} and V_{theor} are constant or slightly decreasing (which is not visible due to the small increase in temperature), due to changes in Gibbs free energy as expressed in Eq. (3).

$$\Delta G°_{rxn,T} = \Delta H°_{rxn,T} - T\cdot\Delta S°_{rxn,T} \tag{3}$$

where $\Delta G°$ is Gibbs free energy, $\Delta H°$ is the enthalpy, $\Delta S°$ is the entropy and T is the operating temperature of the reaction.

Fig. 6 shows the temperature variation of the regions R1-R5 and conventional TCs during the polarisation with the corresponding power output. The regions' temperatures are the average temperature of their corresponding SSPs as shown in Table 1. The represented locations of

the regions, on the other hand, can be seen in the Fig. 2 as circled with black line.

As seen from Fig. 6 the temperature gradient is increased with the increase in drew current resulting in a decrease in voltage. The maximum power density (90 mW cm⁻²) is obtained by multiplying the corresponding cell voltage and current density under the described experimental condition and presented in the Fig. 6. The experimental condition and the size of the used current collector are the driving factor for the obtained cell performance in the current study which is also explained in more detail in Section 3.4.

It is important to note that the prediction of these kinds of small unexpected temperature increments or changes occurring on the cell surface are hard to notice by mathematical modelling which is generally carried out by considering the conventional I-V curve [16]. Since the change/loss in OCV with temperature is negligible they could be attributed to any reasons. However, identifying the temperature dynamics along the cell surface can be vital for thermally induced stresses and their related problems that can lead to detrimental and often non-recoverable damage to the cell [28,29,7,30,31].

3.3. Temperature distribution under loading condition

Fig. 7 shows the temperature distribution obtained from S1-S16 and TCs during loading when 750 mA current is drawn from the system. The experimentally obtained voltage ($Vexpr$) and theoretically calculated Nernst voltage ($Vtheor$) and their correlation with the monitored cathode temperature distribution are plotted in Fig. 6. The furnace temperature was set at 800 °C and a H_2/Air is sent with a constant flow rate of 50 mL min⁻¹ throughout the process. Other cell polarizations including ohmic, activation and concentration losses are not taken into account during the theoretical voltage calculation. Therefore, the decrease in theoretical cell voltage named as $Vtheor$ is due to partial pressure changes of used fuel and oxygen.

The temperature distributions during OCV (with a 50 mL min⁻¹ fuel flow rate) and their changes when 750 mA is drawn from the cell are depicted in Fig. 7. In allowing the electrons to travel from the anode to the cathode, there is a clear increase in temperature due to electrochemical reactions taking place, observed from all SSPs indicating that the cell average temperature is increased. More importantly, the maximum temperature difference among the SSPs S1-S16 during loading increased significantly compared to the difference under the applied OCV condition from about 0.4 °C (between S16 and S5 see Fig. 5) to
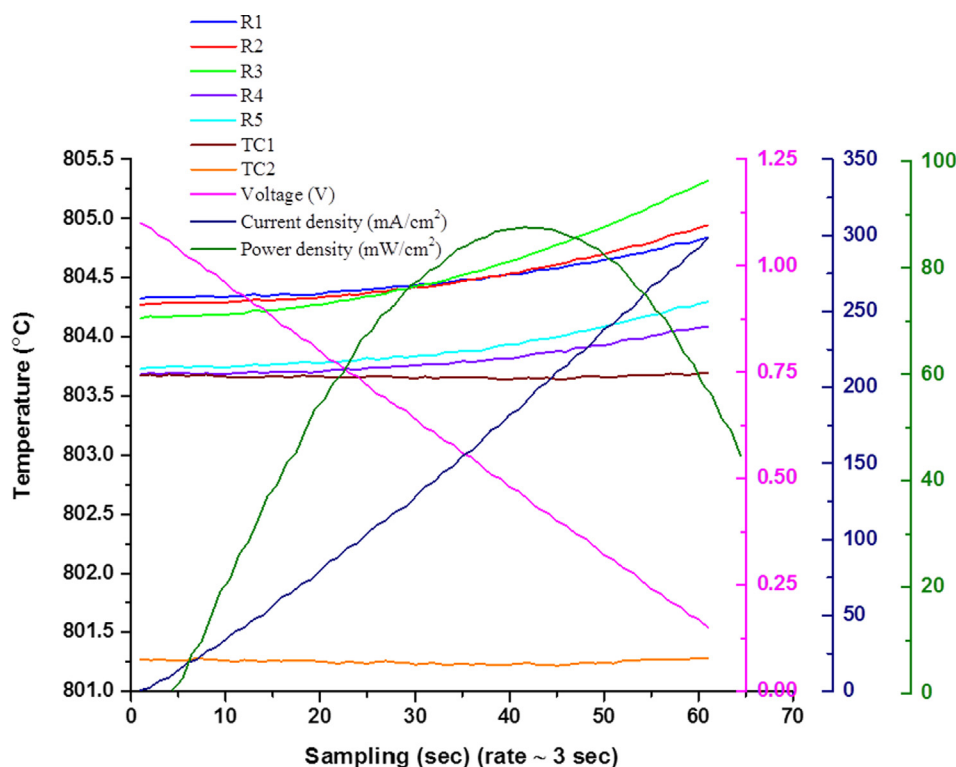
Fig. 6. Variation of local regions temperature during polarisation.

1.35 °C (between S7 and S13 see Fig. 8) while it is decreased for TCs (TC1 and TC2) from 0.06 °C (Fig. 5) to 0.03 °C (Fig. 8). This is because of the higher spatial resolution of the inserted sensor compared to TCs as the measurement is obtained directly from the electrode surface with the sensor while TCs which were placed in the flow channel obtaining the average inside temperature. The observed temperature increments of all SSPs and TCs under the loading condition are plotted in Fig. 8. The temperature increments can be explained with an overall exo-thermic electrochemical reaction as a dominant parameter, joule heating and heat due to resistance to ionic and electronic flow [29]. As can be seen from Fig. 8, the pattern of the measured increments of the SSPs during the loading condition has a relation with the pattern ob-tained during OCV as depicted in Fig. 5.

The SSPs which are located around the silver mesh (S6, S7, S10 and S11) show the maximum rise with an increment of approx. 1.8 °C fol-lowed by S2, S3, S5, S8, S9, S14 and S15 (which are also located close to the current collector but relatively distant from the center) as de-picted in Fig. 8. S1 and S13 show the minimum increment of approx. 0.5 °C (Fig. 8) followed by S4 and S16 which are located on the corner of the cathode. In other words, the four sensing points including S1, S13, S4 and S16 are relatively far from the contact area (between current collector and cathode), which is where it is expected that more electrochemical reactions take place [30]. On the other hand, TC1 and TC2 increased about 0.25 °C and 0.3 °C, respectively, which is less than half of the increment obtained from SSPs S1 and S13 located close to TC1 and TC2, respectively (Fig. 7). The reason for observing higher increment from SSPs located in the center can also be explained as a result of being the point where the electrical wire connection is made,

and hence the first point of concentrated supply of electrons to the cathode. It means that the electrons that are externally transferred from the anode side are starting to reduce the oxygen as soon as they meet the oxygen around the contact point. In analysing Fig. 8, there is an apparent relation observed between the contact area and the tem-perature increments of the cell. The maximum temperature increments are observed near the current collection area as more heat release is expected from where the electrochemical exothermic reaction is taking place [31]. The effect of the heat due to Joule heating and contact re-sistance is less compared to the heat released due to exothermic reac-tions, but their contribution is likely higher near to the current collec-tion area [32]. Regarding this, the results show that the current collection area is found to be a noticeable contributing factor to the given temperature distribution. Due to the shape of the current col-lection area and symmetrically located SSPs, the impact of the current collection area and fuel/air cooling effect(s) are seen from the result. For example, S13, S14, S15 and S16 are located vertically on the same line (Fig. 2), while S14 and S15 are just 1–2 mm away from the current collection area, whilst there is a 10–12 mm distance between S13, S16 and the current collection. The temperature difference between S13 and S14 is around 0.5 °C which is almost the same as the temperature dif-ference between S13 and S4 (fuel inlet and outlet temperature (~42 mm)) under the given condition. This confirms the importance of current collection area effect on the temperature gradient.

At the same time, the fuel flow path is also an important parameter which, for temperature, becomes the limiting factor causing overall output deterioration with the presence of an air gradient [33–35]. In order to observe the effect of the direction of the provided fuel and air

Table 1
Regions and their corresponding SSPs.

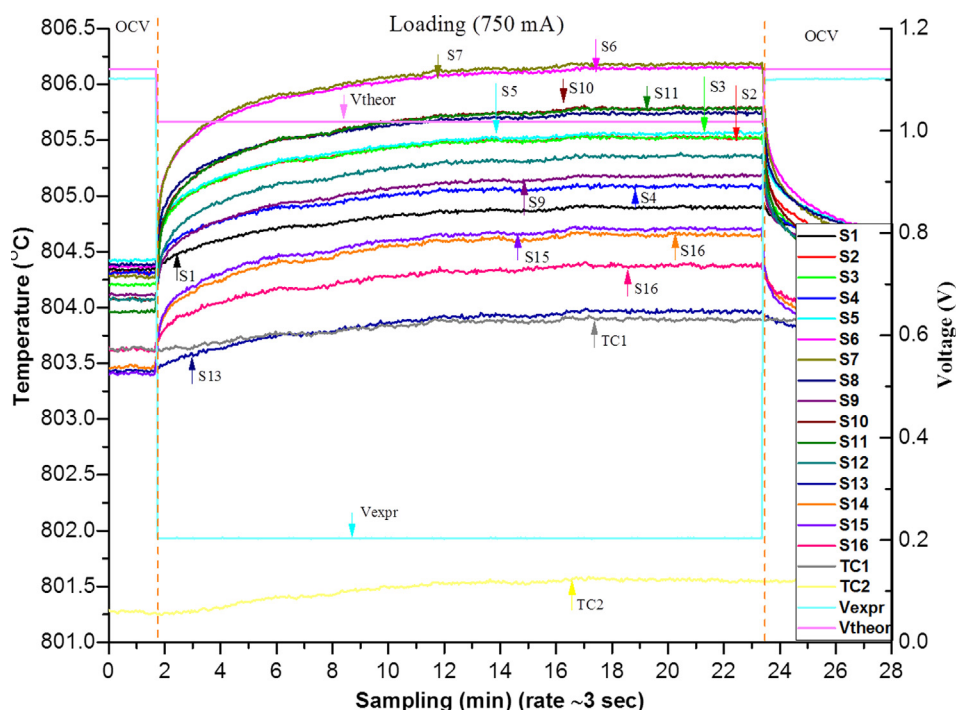| Regions	R1	R2	R3	R4	R5
Corresponding SSPs	Average (S1,S2,S5)	Average (S3,S4,S8)	Average (S6,S7,S10,S11)	Average (S9,S13,S14)	Average (S12,S14,S15)

Fig. 7. Temperature distribution under constant loading condition at 800 °C furnace set temperature.
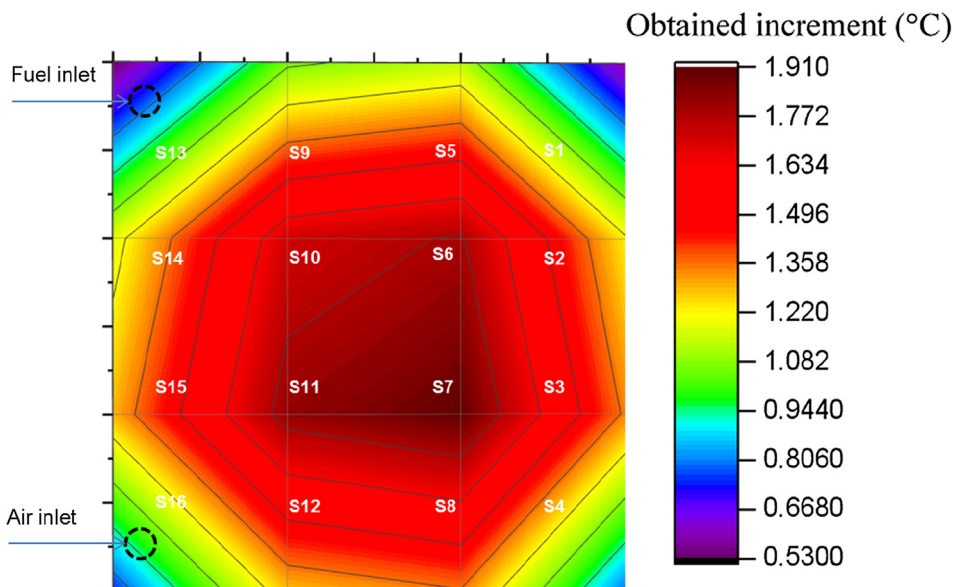

Fig. 8. Temperature increments of sensor sensing points and thermocouples under loading condition.

flow, the SSPs which are placed on the same flow channel and have similar distance to the contact area are compared. In respect to this, S2, S6, S10 and S14 located on the second row and S3, S7, S11 and S15 located on the third row are compared. Since each couple, such as S2 and S3, are on the same flow channel and have similar distance from the contact area, both should experience similar contributions from the electrochemical reaction. As seen from Fig. 8, the obtained increments for the SSPs in the second row are ~0.1 °C less than the increments for their corresponding SSPs on the third row. Similar relations are obtained for the other couples (S6-S7, S10-S11 and S14-S15). Furthermore, the temperature increments for the SSPs on the first row are less than their corresponding SSPs located on the fourth row. There can be two possible reasons for this. These are: (i) that air starvation occurs in the region of the electrode, and/or (ii) the cooling effect by the supplied

fuel (as the fuel is sent along with N_2 leading to a total flow rate of $125\,mL\,min^{-1}$). Since the supplied air has a flow rate of $50\,mL\,min^{-1}$ including only 20% O_2 ($10\,mL\,min^{-1}$ O_2) provided from the bottom-left side corner (see Fig. 2 for location and Fig. 8 for temperature), there is hence the possibility of an insufficient supply of O_2. Thus, this could be the reason for the first row SSPs yielding a slightly lower increment in comparison with their corresponding fourth row SSPs as they could be exposed to air starvation. Normally, air on the cathode side is considered as the main reason for cooling and moreover, it is used to remove the excess heat in the SOFC system [36–38]. Nonetheless the same amount of air and fuel were used in this study to eliminate any possible manipulation from excess air to the temperature distribution. Regarding this finding, it is worth noting that the fuel/air starvation is not only causing performance degradation but also contributing to the

thermal gradient along the cell surface.

Furthermore, in order to analyse the cooling effects of the supplied air, the SSPs located on the left side (S9–S16) and the SSPs on the right side (S1–S8) of the cell are compared by taking into account their distances to the current collector. This is evaluated since the cooling effect due to the supplied gas temperature is considered as another contributor to temperature gradient in SOFC systems [33,34]. As seen from Fig. 8, the SSPs located on the left side of the cell show a slightly lower temperature increment than their corresponding SSPs located on the right side of the cell. For instance, S2 and S3 show slightly higher increments than their corresponding sensing points S14 and S15, respectively. This is due to the air cooling effect as S14 and S15 are closer to the air inlets which are affected more than S2 and S3. The differences between the obtained temperature increments from these symmetric SSPs are negligibly small (~0.1 °C). This information is also providing knowledge about distinguishing individual impact of aforementioned parameters contributing to the cell temperature increments, namely that the cooling effect under these flow conditions are minimal when compared to the location of the manifold with regards to the furnace wall, and the fuel/air starvation effects.

3.4. Thermodynamic analysis of the obtained temperature increment during loading

The relationship between the operating temperature and cell voltage has already been mentioned in the above sections. Thus, in this section the corresponding temperature increment from the released heat is theoretically calculated to compare the experimentally obtained temperature variations. By taking into account the described experimental condition, the data from the experimentally obtained I-V curve is applied as the main source during the calculation. Hence, Eqs. (4)–(6) are derived for the relationships between the I-V correlated data and the corresponding released heat from the reactions. Specifically, in this experiment, the temperature increment due to the heat release from the electrochemical exothermic reaction is the focus. Thus the Eq. (4) is performed to calculate the reacted molar flow of H_2 depending on the drawn current density and the equivalent fuel flow rate at both the anode and cathode electrodes under the loading condition [39].

$$250 \frac{mAmps}{cm^2} \left(\frac{mC}{s.cm^2} \right) \times \frac{1 \ mol \ e^-}{96485 \ C} \times \frac{1 \ mol \ H_2}{2 \ mol \ e^-}$$

(4)

$$Reacted \ molar \ H_2 = 1.3 \times 10^6 \left(\frac{mol}{s.cm^2} \right)$$

$$\rightarrow equivalent \ H_2 \ flow \ rate \ found \ as \ 5.2 \ mL \ min^{-1}$$

$$Reacted \ molar \ O_2 = 0.65 \times 10^6 \left(\frac{mol}{s.cm^2} \right)$$

$$\rightarrow equivalent \ O_2 \ flow \ rate \ found \ as \ 6.8 \ mL \ min^{-1}$$

The total gas sent to the cathode side is 50 mL min^{-1} air which includes a 10 mL min^{-1} O_2 flow rate. The utilisation of the O_2 is calculated as 68%. As previously discussed, O_2 is a limiting factor in this experiment which allows investigation into the fuel starvation- based effect on temperature distribution. Additionally, the utilisation of H_2 is calculated as about 10% which is critically low and is the main reason for a relatively low power density (Fig. 6). It should be reiterated that the main focus of this study is not directly concerned with the cell optimum performance, it is instead the temperature profile under given conditions, which have been specifically skewed in terms of flow rates and current collector area to induce/exacerbate the temperature increments, as well as to demarcate the different causes and effects.

The molar flow of the reacted H_2 is calculated from the equation given in (4) by using the drawn current density. Regarding this, Table 2 illustrates the percentage of excess gas out of the total feed gases on both the anode and cathode chamber separately. This is important to determine, given the fact that the higher the amount of excess gases, the

Table 2
Flow rate of supplied gases and percentage of the excess gases.

	Total gases flow rate sent (mL min^{-1})	Percentage of excess fuel
Anode	125 (H$_2$ (50), N$_2$ (75))	96%
Cathode	50 (Air)	86%

greater the likelihood and proportion of a cooling effect on the measured temperature increment. From the other side, the lower utilisation of H_2 is because of the small cell active area used which is limited by the small-sized current collector (~3 cm^2).

The given formulas in Eq. (5) [29] and (6) [40] for the released corresponding heat from the electrochemical reaction and net resultant heat after the effect of heat losses is considered.

$$Q_e = R_e \Delta H_f - I_{cell} E_{cell} + \frac{I_{cell}^2}{\sigma}$$

(5)

where Q_e (J s^{-1}) is the released heat rate for cell area (heat flux) from the electrochemical reaction, R_e is the molar flow, ΔH_f (J mol^{-1}) is enthalpy of the formation at the given temperature, I_{cell} (Amps cm^{-2}) is the current density, $Vexpr$ (V) is the voltage of the operating cell and σ is taken as the bulk ionic conductivity of the YSZ electrolyte for joule heating purposes calculated at roughly 3 Sm^{-1} [41].

$$\Delta Q = Q_e - Q_{conv} = mc_p \Delta T$$

(6)

ΔQ (J) is net heat that increases the cell temperature, Q_{conv} (J) is the heat lost, m is the mass of the cell, C_p is the specific heat capacity (J g^{-1} K^{-1}) of the cell and ΔT (K) is the time dependent temperature difference between cell solid (T_s) and fuel (T_f) phase in the anode and cathode channel.

$$Q_{conv} = h \, A \, \Delta T \ [\Delta T = (T_s - T_f)]$$

(7)

It is worth noting that the local thermal equilibrium (LTE), referring to the negligible heat transfer from the solid to gas phase within the porous electrode, is considered during the analytical calculation [42]. A heat loss via convection due to advection of the excess gases through the fuel flow channels is assumed as the main reason for heat consumption. Additionally, heat contributions of cell overpotential losses are inherently taken into account in Eq. (5), by using the product power of the measured cell voltage and current density, in lieu of the product of activation and concentration overpotentials with current density. The joule heating term yields a value of approximately 0.024 W and is henceforth neglected in the analysis. Heat losses via conduction through the cell gasket and manifolds are not directly calculated by per-component basis, due to complexity of determining the exact contact boundaries of the components. Instead, their effects are brought to bear via time-dependent analysis of the thermal gradients, as to which body or bodies are acting as heat conducting and absorbing masses.

If it is assumed that all the released heat is consumed or coming out due to convection, then the maximum temperature difference can be calculated

$$Q_{net} = Q_{in} \left(\frac{J}{s} \right) - Q_{conv} \left(\frac{J}{s} \right)$$

(8)

$$mc_p \Delta T = 0.273 - 0.033 \Delta T$$

From Eq. (8) the rate of the temperature difference is calculated as 0.06 °C s^{-1} with the assumption of $m = 9$ g and $c_p = 0.5$ J g^{-1} K^{-1}. The calculated value is well aligned with the experimentally obtained increment from the SSPs especially for the first gradient shown in Fig. 9. The small difference in experimentally measured and analytically calculated increment can be attributed to the heat dissipated by convection to the gas phase within the porous electrodes which is not considered in this study during the theoretical calculation. There are also contributions to heat loss from conduction via SOFC solid components which are in physical contact with cell, such as gasket materials and
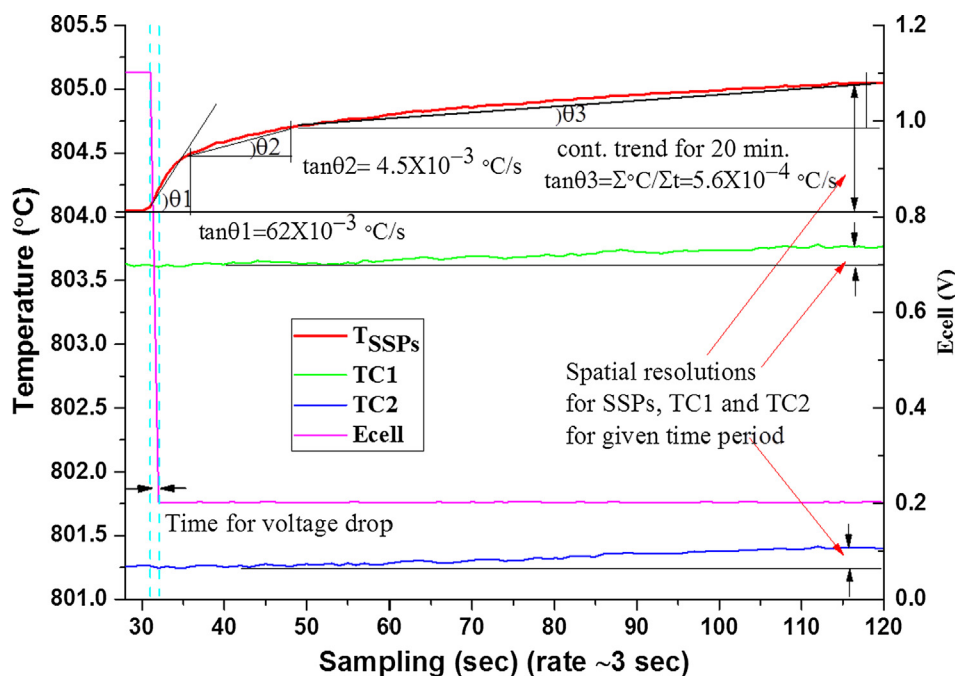
Fig. 9. Obtained average temperature increment from SSPs and TCs under varying operating condition.

ribs of manifolds, and also due to radiation, both of which are neglected during the calculation. The impact of these parameters is exerting greater influence with time, being more considerable since the heat is transferred through the whole bodies of a cell manifold system. Thus, there is great difference in the calculated increment rate and the rate measured when the system starts reaching the thermal equilibrium (tanθ2 and tanθ3). However, overall, the experimentally obtained increment is promising and shows good agreement with the analytically calculated increment. Three different transient conditions are defined for the monitored time-dependent temperature variation depending on the gradient (tanθ1, tanθ2, tanθ3) as depicted in Fig. 9. The greatest gradient (tanθ1) is observed just after the system is loaded, which is about twelve times greater than the second gradient (tanθ2). If the assumption is held that the cell is the sole body for heat absorbed in the time duration described by gradient tanθ1, with m = 9 g, Eq. (8) yields a temperature increment of 30 °C after 500 s, which can continue to rise with time if the rate is maintained; this is not the case from the observed experimental readings. This is manifested in the period with the gradient tanθ2, which shows a decrease in the rate (from $\sim 62 \times 10^{-3}$ °C/s to 4.5×10^{-3} °C/s). The third gradient (tanθ3), on the other hand, is extremely low compared to two previous gradients. By this time, the generated heat is held not only by the cell, but instead is held by the whole body of the cell manifold arrangement/assembly as the system is approximately reaching the steady-state condition during this period (Fig. 9). Thus, the left side of the Eq. (8) is required to be modified for realistic analytical temperature increment when the system is nearing the thermal equilibrium. In the literature for modelling concerning temperature increments, the obtained values are varying in the region of 60–120 °C; this is mainly due to variances in experimental parameters such as fuel utilisation(> 60%), [43,44] drawn current density (much greater than the drawn current density from this experiment) and sizes and properties of cell and manifold. In particular, the manifold/interconnect is a single block in our presented work, but simulations are conducted with very thin interconnect geometry [43,44]. It is also possible to determine the difference between the temporal resolution of SSPs and conventional TCs by the calculated gradients in which there is not any visible temperature increment monitored from the TCs for first and second gradients. Comparatively, the observed spatial resolution of SSPs for a given time range is at least six times higher than the TCs as shown in the Fig. 9.

A quicker response of temperature increment is monitored from SPPs when the system is loaded in comparison with the conventional TCs (Fig. 9). The cell voltage, *Vexpr*, drops to a settled voltage of 0.2 V from the operating OCV voltage of 1.1 V in about 1 s. It is difficult to talk about a precise steady state condition if there are complex and continuous heat release/sink mechanisms such as those in a SOFC. The heat release/sink mechanism of a SOFC system is affected by some complex parameters including electrochemical and chemical reactions, overpotential losses, and heat losses via radiation, convection and conduction. Therefore, the period where the varying sharp increases are monitored can be referred to as the transient condition whilst the period where the slight increase is monitored is can be referred to as the partially steady state condition. As seen from Fig. 9, the temperature increment starts as soon as the system is loaded since the SSPs are located directly on the cell surface and the temperature difference between holes and the solid body of the cell is negligible [42]. The observed thermal gradient along the cell surface under the given condition can be considered as negligible (at about 1.5 °C). This is because of the small temperature increase caused from loading due to small sized current collector and cell. However, the relationships between current collection area, fuel/air flow direction and cooling effect with the temperature increment is monitored sensitively and independent from the level of the rate of the increment, that is to say applicable for other experimental conditions. It is reiterated that current collection area and air (oxygen) concentration across the cell are found as more dominant parameters rather than H_2 concentration or inlet/outlet locations.

In addition to this, there is a greater difference in average temperature increments obtained from SSPs and TCs. This difference increased significantly during loading compared to the increments observed during the OCV condition. The average increments obtained from SSPs (1.25 °C) is approx. five times higher than the average increment obtained by TCs (0.25 °C) during loading. If it is assumed that those values for the temperature increment would be further increased in proportion with the cell and current collector being enlarged, this can be an important difference that can mislead the modeller if the data from TCs is used for validation purposes. This is especially true in the case of having higher thermal gradients as the gradient can further increase depending on the experimental condition, and hence it can be

of vital importance to have more realistic temperature measurements. With regards to the obtained temperature distribution, the given cell size, amount of drawn current, fuel and air flow types, cell materials, manifold or stack design, and even furnace configuration are important parameters that influence the thermal gradient of the SOFC at both cell and stack levels. As is addressed in the literature [38] there is a strong relationship between those mentioned physical parameters and SOFC operating performance. The effect can be expected to be more pronounced at the stack level. With the variation of those parameters the temperature distribution can be significant [40,42]. In respect to this, the presented method has great potential to address the individual source of the released/sink heat during operation with having the advantages of higher spatial and temporal resolution compared to the conventional measurement obtained from the flow channel with TCs. Having higher resolution in temperature sensing is significantly important for *in-situ* monitoring of SOFC operation, not only for identifying temperature-related issues such as thermal stress related cracks but also for kinetics of chemical and electrochemical reactions, distinguishing the overpotential-related losses, gas distribution and fuel utilisation. With the further improvement in the proposed sensor implementation by minimising its disturbance to the working environment, the method can provide more benefits in other forms, such as *in-situ* health monitoring diagnostics tools for SOFCs performance degradation. A self-sustained system for sensor will be developed and the sensor will be tested to provide the temperature-related information from a single cell as well as stacked SOFCs modules. The modelling approaches considered here are also quite rudimentary in comparison to the available literature, and so we aim to present this work as a first step for further computational analysis and verification performed in conjunction. Work is also being performed to use sensor-obtained data for simulation and validation of machine learning routines for the identification of failures and the viability of this method as a state-of-health monitoring tool.

4. Conclusions

Temperature distribution of an anode-supported SOFC and its changes under OCV and loading conditions is monitored by the cell-implanted SSPs which are in direct contact with the cathode surface. Two commercial TCs are also used to compare the measurement obtained with SSPs from the same location in order to investigate the capability of this sensory technique in terms of temporal and spatial resolution. Under OCV conditions, temperature increments due to fuel/air flow rate increase were detected well by SSPs and TCs with only a small difference among them. There is a small temperature variation observed along the cathode surface due to the sensing point's location. The increase in the measured temperature with increase in flow rate, as attributed to the direct fuel oxidation due to small gas leakage, is observed by the SSPs located on the outer side of the cathode. On the other hand, under loading conditions, TCs were found not to be sensitive to the temperature increments caused by cell electrochemical activities when compared to the increments monitored by the SSPs. The obtained temperature increment is compared with the theoretically calculated increment by using the *I-V* related thermodynamic and loading information. Good similarity is observed between the experimental and theoretical temperature increment until the sensors reach thermal balance. Current collector contact area was found as the dominant factor resulting in temperature variation under loading conditions, being considered with the impact of gas cooling and flow direction effects. Furthermore, there are other factors that should be taken into account for analysing temperature variation across the cell electrodes, such as (i) the position of the manifold which can be influenced by uneven temperature distribution within the furnace, (ii) the presence of gas crossover leading to direct chemical oxidation of fuel, (iii) reactant starvation and finally (iv) cooling effects of supplied air. It is established that for the given conditions, the cooling effects were relatively subdued in contributing to the temperature variation. In respect to the findings, the measurement directly from the cell surface is considered as a more realistic way to understand the temperature phenomena of the SOFC operation in comparison to the TC-based measurement from the flow channel as an experimental method. Sensitive detection of the local temperature variations allows definition of the origin of the sources of either heat releases or losses. This would help to diagnose the problems induced by high operating temperature before possible system failure.

References

[1] Wang Y, Cai L, Liu T, Wang J, Chen J. An efficient strategy exploiting the waste heat in a solid oxide fuel cell system. Energy 2015;93:900–7.
[2] Xu H, Chen B, Tan P, Cai W, He W, Farrusseng D, et al. Modeling of all porous solid oxide fuel cells. Appl Energy 2018;219(February):105–13.
[3] Lee K, Kang S, Ahn KY. Development of a highly efficient solid oxide fuel cell system. Appl Energy 2017;205(April):822–33.
[4] Tanasini P, Cannarozzo M, Costamagna P, Faes A, Van Herle J, Hessler-Wyser A, et al. Experimental and theoretical investigation of degradation mechanisms by particle coarsening in sofc electrodes. Fuel Cells 2009;9(5):740–52.
[5] Yan D, Zhang C, Liang L, Li K, Jia L, Pu J, et al. Degradation analysis and durability improvement for SOFC 1-cell stack. Appl Energy 2016.
[6] Chao C-C, Hsu C-M, Cui Y, Prinz FB. Improved solid oxide fuel cell performance with nanostructured electrolytes. ACS Nano 2011;5(7):5692–6.
[7] Zeng H, Wang Y, Shi Y, Cai N, Yuan D. Highly thermal integrated heat pipe-solid oxide fuel cell. Appl Energy 2018;216(February):613–9.
[8] Ormerod RM. Solid oxide fuel cells. Chem Soc Rev 2003;32(1):17–28.
[9] Tucker D, Abreu-Sepulveda M, Harun NF. SOFC lifetime assessment in gas turbine hybrid power systems. J Fuel Cell Sci Technol 2014;11(5):51008.
[10] Al-Masri A, Peksen M, Blum L, Stolten D. A 3D CFD model for predicting the temperature distribution in a full scale APU SOFC short stack under transient operating conditions. Appl Energy 2014;135:539–47.
[11] Hashimoto S, Nishino H, Liu Y, Asano K, Mori M, Funahashi Y, et al. The electrochemical cell temperature estimation of micro-tubular SOFCs during the power generation. J Power Sources 2008;181(2):244–50.
[12] Guo H, Iqbal G, Kang BS. Development of an in situ surface deformation and temperature measurement technique for a solid oxide fuel cell button cell. Int J Appl Ceram Technol 2010;7(1):55–62.
[13] Barelli L, Bidini G, Cinti G, Ottaviano A. SOFC regulation at constant temperature: Experimental test and data regression study. Energy Convers Manage 2016;117:289–96.
[14] Montanini R, Quattrocchi A, Piccolo SA, Amato A, Trocino S, Zignani SC, et al. Real-time thermal imaging of solid oxide fuel cell cathode activity in working condition. Appl Opt 2016;55(25):7142.
[15] Ota T, Koyama M, Wen CJ, Yamada K, Takahashi H. Object-based modeling of SOFC system: Dynamic behavior of micro-tube SOFC. J Power Sources 2003;118(1–2):430–9.
[16] Aydın Ö, Nakajima H, Kitahara T. Reliability of the numerical SOFC models for estimating the spatial current and temperature variations. Int J Hydrogen Energy 2016;41(34):15311–24.
[17] Liso V, Cinti G, Nielsen MP, Desideri U. Solid oxide fuel cell performance comparison fueled by methane, MeOH, EtOH and gasoline surrogate C8H18. Appl Therm Eng 2016;99:1101–9.
[18] Guk E, Ranaweera M, Venkatesan V, Kim J-S. Performance and durability of thin film thermocouple array on a porous electrode. Sensors 2016;16(9):1329.
[19] Ju G, Reifsnider K, Huang X. Infrared thermography and thermoelectrical study of a solid oxide fuel cell. J Fuel Cell Sci Technol 2008;5(3):31006.
[20] Ranaweera M, Kim JS. Cell integrated multi-junction thermocouple array for solid oxide fuel cell temperature sensing: N + 1 architecture. J Power Sources 2016;315:70–8.
[21] Pollock DD. The theory and properties of thermocouple elements. Philadelphia; 2015.
[22] Son JW, Song HS. Influence of current collector and cathode area discrepancy on performance evaluation of solid oxide fuel cell with thin-film-processed cathode. Int J Precis Eng Manuf - Green Technol 2014;1(4):313–6.
[23] Rolle A, Thoréton V, Rozier P, Capoen E, Mentré O, Boukamp B, Daviero-Minaud S. Evidence of the current collector effect: study of the SOFC cathode material Ca$_3$Co$_4$O$_{9+\delta}$. Fuel Cells Apr. 2012;12(2):288–301.

[24] Chiodelli G, Malavasi L. Electrochemical open circuit voltage (OCV) characterization of SOFC materials. Ionics (Kiel) 2013;19(8):1135–44.

[25] Xu M, Li TS, Yang M, Andersson M, Fransson I, Larsson T, et al. Modeling of an anode supported solid oxide fuel cell focusing on thermal stresses. Int J Hydrogen Energy 2016;41(33):14927–40.

[26] Bhattacharyya D, Rengaswamy R. A review of solid oxide fuel cell (SOFC) dynamic models. Ind Eng Chem Res 2009;48:6068–86.

[27] Matsui T, Inaba M, Mineshige A, Ogumi Z. Electrochemical properties of ceria-based oxides for use in intermediate-temperature SOFCs. Solid State Ionics 2005;176(7–8):647–54.

[28] Jiang W, Luo Y, Zhang W, Woo W, Tu ST. Effect of temperature fluctuation on creep and failure probability for planar solid oxide fuel cell. J Fuel Cell Sci Technol 2015;12(5):51004.

[29] Ho TX, Kosinski P, Hoffmann AC, Vik A. Effects of heat sources on the performance of a planar solid oxide fuel cell. Int J Hydrogen Energy 2010;35(9):4276–84.

[30] Jin L, Guan W, Niu J, Ma X, Wang WG. Effect of contact area and depth between cell cathode and interconnect on stack performance for planar solid oxide fuel cells q. J Power Sources 2013;240:796–805.

[31] Metzger P, Friedrich KA, Muller-Steinhagen H, Schiller G. SOFC characteristics along the flow path. Solid State Ionics Notes 2006;177(19–25):2045–51.

[32] Dillig M, Biedermann T, Karl J. Thermal contact resistance in solid oxide fuel cell stacks. J Power Sources 2015;300:69–76.

[33] Razbani O, Wærnhus I, Assadi M. Experimental investigation of temperature distribution over a planar solid oxide fuel cell. Appl Energy 2013;105:155–60.

[34] Zaccaria V, Tucker D, Traverso A. A distributed real-time model of degradation in a solid oxide fuel cell, part II: Analysis of fuel cell performance and potential failures. J. Power Sources 2016;327:736–42.

[35] Park J, Kang J, Bae J. Computational analysis of operating temperature, hydrogen flow rate and anode thickness in anode-supported flat-tube solid oxide fuel cells. Renew Energy 2013;54:63–9.

[36] Baldinelli A, Barelli L, Bidini G, Di Michele A, Vivani R. SOFC direct fuelling with high-methane gases: Optimal strategies for fuel dilution and upgrade to avoid quick degradation. Energy Convers Manage 2016;124:492–503.

[37] Severson H, Assadi M. Analysis of residual and operational thermal stresses in a planar SOFC. J Fuel Cell Sci Technol 2013;10(6):61001.

[38] Andersson M, Yuan J, Sundén B. SOFC modeling considering electrochemical reactions at the active three phase boundaries. Int J Heat Mass Transf 2012;55(4):773–88.

[39] Kaur G. Solid oxide fuel cell components: interfacial compatibility of SOFC glass seals. In: Solid oxide fuel cell components: interfacial compatibility of SOFC glass seals; 2015. p. 1–408.

[40] Abbas MR, Noor AM, Rajoo S, Ahmad N, Basheer UM, Sah MHM. Thermal conductivity and specific heat capacity of different compositions of Yttria stabilized zirconia-nickel mixtures. Adv Mater Res 2015;1119(April):783–8.

[41] Pramuanjaroenkij A, Kakaç S, Yang Zhou X. Mathematical analysis of planar solid oxide fuel cells. Int J Hydrogen Energy 2008;33(10):2547–65.

[42] Damm DL, Fedorov AG. Local thermal non-equilibrium effects in porous electrodes of the hydrogen-fueled SOFC. J Power Sources 2006;159(2):1153–7.

[43] Andersson M, Paradis H, Yuan J, Sunden B. Three dimensional modeling of an solid oxide fuel cell coupling charge transfer phenomena with transport processes and heat generation. Electrochim Acta 2013;109:881–93.

[44] Shi Y, Wang H, Cai N. Direct two-dimensional electrochemical impedance spectra simulation for solid oxide fuel cell. J Power Sources 2012;208:24–34.